Chapter 1

Finite-Element Modeling of the Growth and Interaction of Hydraulic Fractures in Poroelastic Rock Formations

Adriana Paluszny[1], Saeed Salimzadeh[2], Robert W. Zimmerman[1]
[1]*Imperial College, London, United Kingdom;* [2]*Technical University of Denmark, Lyngby, Denmark*

1.1 INTRODUCTION

Many analytical models have been developed to investigate different aspects of the hydraulic fracturing process. These models have proved to be very useful in identifying the important factors that influence hydraulic fracture growth and elucidating their effect on the created fracture radius and aperture. However, in general, such models cannot simultaneously account for multiple factors, such as matrix permeability and thermal effects. Furthermore, such models generally take the form of asymptotic solutions, which can be accurate in extreme regions of the parameter space (i.e., viscosity dominated or toughness dominated), but are not accurate in intermediate cases. Finally, analytical solutions are difficult to obtain in situations involving the growth of multiple fractures from a single borehole. Hence, there is a need for a robust numerical approach that can accurately handle all geometries and parameter ranges.

In the broader context of rock fracturing, not necessarily restricted to man-made hydraulic fractures emanating from pressurized boreholes, numerical methods can be extremely useful in understanding the effects of in situ conditions, rock properties, and heterogeneities on the geometric and topological characteristics of fracture networks and their effect on mechanical and flow properties of the rock. Numerical approaches to model fractures within a continuum can be classified into (1) nongeometric methods, in which the fracture is represented as a material property of the mesh, including localized damage and plastic models and (2) geometric methods, in which each fracture is represented explicitly and occupies a volumetric or surface domain that is distinct from the rock matrix. This chapter will focus on geometric methods in

1

which fractures are represented by surfaces and rock property heterogeneities are represented explicitly in the models.

Numerous recent studies have attempted to model fracture propagation in 3D. Nongeometric fracture growth models look at the transition between grain-scale microcracking and cm-scale mesoscale cracking and are generally referred to as "damage" models (Patzák and Jirásek, 2004). These are also known as subgrid or nongeometric models, because they represent multiple "smaller" fractures within a single finite-element triangle or tetrahedron, and therefore do not explicitly represent individual cracks. Phenomenological damage models are material specific, in situ condition specific, and are based on a postulated fracture evolution law. Thus, they have to be fitted to experimental data to be usable. Another type of nongeometric approach is the family of so-called "meshfree" crack methods, including cracking particles, which keep track of fractures implicitly by tagging nodes as being "cracked" during fracture growth (Rabczuk and Belytschko, 2007). These methods also do not explicitly represent individual cracks and rely on secondary reconstruction mechanisms to track fracture surfaces and fronts. Existing multiscale models, such as the "classical" and "cohesive" multiscale models, developed to upscale microfracturing damage models, are based on the existence of a representative elementary volume (REV) (Vernerey and Kabiri, 2014). However, these models break down when applied to quasi-brittle rocks, for which REVs can rarely be identified above the centimeter scale, as fractures tend to exist at all length scales. A multiscale approach must consider both the existence of small scale, microstructure-dependent fractures, as well as the discrete fracture growth of larger fractures.

Discrete fracture growth models are geometric methods that represent fractures "discretely"; they assume that fractures have a body and geometry that change during growth. Such models can make use of a variety of numerical methods, such as the boundary element method (Carter et al., 2000), the finite-element method (Paluszny and Zimmerman, 2011), and the extended finite-element method (Bordas et al., 2008). The finite-element approach defines fracture geometry as part of the mesh, whereas the extended finite element represents fractures as discontinuities that exist within elements of the mesh. The extended finite-element method is constrained in that it allows for only one fracture orientation per element and has a limited "level set" amount of predefined fracture orientations. The finite-element method is, in contrast, more flexible if used as an instrument to inform the growth of a geometric model, as in, for example, the method recently developed by Paluszny and Zimmerman (2011). Models based on stress intensity factors (SIFs) are not generally suited to study smaller scale damage, due to their elevated computational cost and continuity assumptions. However, an innovative method has recently been developed (Paluszny and Zimmerman, 2011) that allows energy-based computations to be carried out on coarse unstructured meshes, without requiring a brick-like mesh, and enables one to model the growth of multiple fractures simultaneously, in three dimensions (Paluszny et al., 2013; Nejati et al., 2015b), at a variety of scales.

1.2 COMPUTATIONAL FRAMEWORK

In this chapter, a numerical framework to model the growth of multiple fractures in three dimensions is described. Fractures are represented discretely, using three-dimensional nonplanar surfaces that are embedded in three-dimensional volumetric domains representing the rock. The framework is suitable for both porous and nonporous rocks. By capturing fracture geometry using surfaces, their high aspect ratio is preserved, and both their geo-mechanical and flow behavior can be modeled independently in a simultaneous manner. Fractures are represented volumetrically, in the sense that each fracture disk is represented by two superimposed surfaces. Thus, the fracture represents a true discontinuity in the mechanical deformation model. Contact between these surfaces is modeled as part of the simulation, as is the fluid flow through the fracture and the leakoff from the fracture to the matrix. The separation of the fracture walls is tracked during the simulation, yielding a detailed distribution of fracture apertures across the fracture surface. Thus, the aperture distribution on the fracture surface changes as the fluid advances through the fracture and interacts with the in situ stresses. This fracture aperture distribution affects the permeability of the fracture, and in the context of hydraulic fracturing, it also affects the transfer of heat between fracture and matrix, as well as the fluid flow from fracture to matrix. Consequently, it affects the resulting patterns of fractures in a multifracture system.

The rock is assumed to be a linear, elastic, and homogeneous material. In the case of hydraulic fracturing, the main two boundary conditions are the fluid pressure within the fractures and the remote in situ stresses. In addition, a temperature contrast between the fluid and rock can also be accounted for. At each iteration, the thermoporoelastic deformation field is computed. The deformation field depends on the fluid, mechanical, and thermal behavior of both the rock and fluid. A flowchart of the computational procedure is shown in Fig. 1.1.

Energy-based approaches for fracture growth compute SIFs, which can be computed for each fracture modality (I tensile, II and III shear), and can then be directly compared with the toughness of the rock, at different scales. SIFs are measures of the elastic energy change due to fracture growth and are computed at each fracture tip node. By using isoparametric quarter-point elements around the fracture tips (Nejati et al., 2015b), these SIFs can be computed with great accuracy for relatively coarse meshes and result in fracture growth predictions that are independent of both the mesh structure and the mesh refinement. Based on these SIFs, predictions of growth direction and magnitude are made, and the geometric growth of the fracture is computed. At each tip node, a growth vector is computed, resulting in a distributed growth prediction for each fracture. Thus, the numerical framework can capture a scenario in which part of the fracture may be subjected to tension, while another is being subjected to shear, for example. This may result in a variation
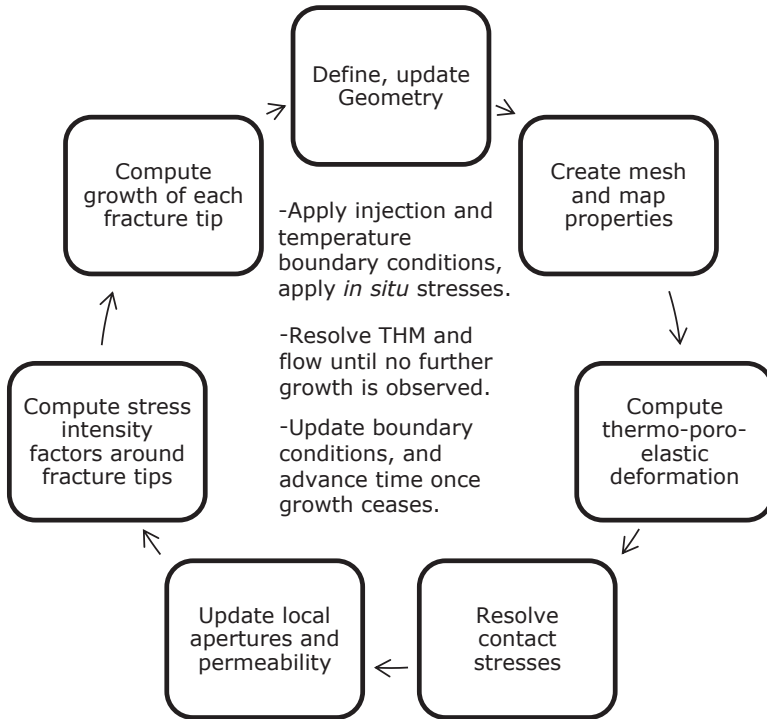
FIGURE 1.1   Schematic representation of the simulation workflow. The numerical framework is based on the finite-element method and assumes that the fractures are represented explicitly by the mesh. Each fracture is composed of two initially overlapping surfaces that may either separate or contact during the deformation. Apertures are computed locally, deformation is poroelastic, and fluid flow is modeled using Darcy's law.

of radii and growth angles across the fracture tip. At each fracture tip node, the direction of fracture propagation is computed from an experimentally validated mixed mode 3D fracture angle criterion that is based on the maximum circumferential stress (Schöllmann et al., 2002). In addition, at each node, the extent of growth is computed independently as a function of the SIFs, relying on semianalytical Paris-type functions that can capture growth modes ranging from brittle to fatigue behavior, by using a material-specific propagation exponent (Lazarus, 2003). This results in fractures that may grow out of their initial plane, if the growth criteria thus specify. This local process is repeated for each fracture, around its tip curve, and for each tip node, in an individual manner. Therefore, multiple fractures can be assessed simultaneously using the same approach, and the interaction between nearby fractures is an emerging behavior of the simulation. Examples of the growth of multiple fractures in 3D are shown in Fig. 1.2.

(A)

(B)
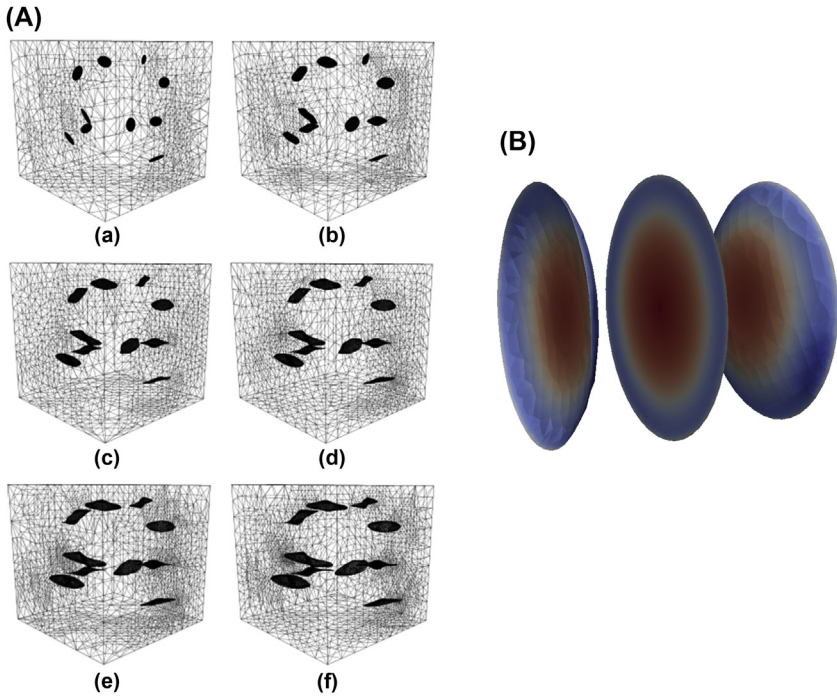
FIGURE 1.2   Example of modeling of the growth fractures using the present numerical framework. (A) Ten fractures grow under tension; (B) three hydraulic fractures grow simultaneously during injection.

1.3 MODELING OF THERMOPOROELASTIC DEFORMATION IN FRACTURED MEDIA

The fully coupled thermohydromechanical (THM) model consists of six interacting submodels and the numerical model for integrated fracture growth prediction. The separate THM submodels are three heat transfer models, two flow models, and the thermomechanical model. Separate flow models are defined for the rock matrix and the fractures, to accurately capture hydraulic loadings on the fracture surfaces, as well as the poroelastic deformation of the deformable rock matrix, and are coupled using fluid leakage terms (Fig. 1.3). The THM scheme to compute temperature, fluid pressure, and displacements at the nodes of the matrix and fractures is a monolithic, fully coupled, three-dimensional finite element−based approach described in detail by Salimzadeh et al. (2017a,b). The presented simulations are for single-phase flow, but the method can be extended to include the effects of multiphase flow within the same framework.

Fluid properties typically vary nonlinearly, and over several orders of magnitude, with changing pressure and temperature. Initially, fluid properties are obtained using lookup tables based on the IAPWS (International
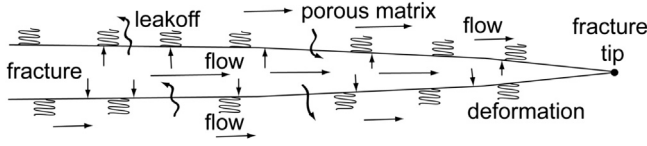
FIGURE 1.3 Schematic representation of the fracture and interaction between the governing equation for (1) mechanical deformation, (2) fluid flow in the fracture, and (3) fluid flow in the matrix.

Association for the Properties of Water and Steam; www.iapws.org) pure water equation of state. For cases where more complex equation of state data are available, these can be incorporated into the simulation. Pressure and temperature equations are solved using a finite-element finite-volume method (FE-FV), in which advective parts of the equations are solved using the finite-volume method and diffusive parts are solved using the finite-element method. Details of this scheme are available in Paluszny et al. (2007). The deformation of the matrix due to stress, temperature, and fluid pressure is governed by the thermomechanical model's governing equation

$$
\iiint_\Omega \left\{ \operatorname{div}\left[\frac{1}{2}\mathbf{D}(\nabla\mathbf{u} + \mathbf{u}\nabla) - \alpha p_m \mathbf{I} - \beta_s K(T_s - T_{s0})\mathbf{I} \right] + \mathbf{F} \right\} dV - \iint_{\Gamma_c} p_f n_c dS = 0
$$

$$(1.1)$$

where $\mathbf{D}$ is the drained stiffness tensor, $\mathbf{u}$ is the displacement vector of the rock solid, α is the Biot coefficient of the matrix, p_m is the matrix fluid pressure, $\mathbf{I}$ is the identity tensor, β_s is the volumetric thermal expansion coefficient of the matrix, K is the bulk modulus of the porous rock, T_s is the current temperature of the solid rock, T_{s0} is the initial temperature of the solid rock, $\mathbf{F}$ is the body force vector per unit volume, p_f is the fluid pressure in the fracture, n_c is the outward unit normal vector to the fracture surface, Ω is the region occupied by the rock mass, and Γ_c is the boundary of the fracture (Zimmerman, 2000).

The first flow model describes flow within the matrix as follows (Salimzadeh and Khalili, 2015):

$$
\iiint_\Omega \operatorname{div}\left[\frac{\mathbf{k}_m}{\mu_f}(\nabla p_m + \rho_f g) \right] dV
$$

$$
= \iiint_\Omega \left\{ \alpha \frac{\partial(\operatorname{div}\mathbf{u})}{\partial t} + \left[\phi c_f + \frac{(\alpha - \phi)}{K_s} \right] \frac{\partial p_m}{\partial t} - \phi\beta_f \frac{\partial T_m}{\partial t} \right\} dV + \iint_{\Gamma_c} c_L(p_m - p_f) dS
$$

$$(1.2)$$

where $\mathbf{k}_m$ is the permeability tensor of the matrix, μ_f is the fluid viscosity, ρ_f is the fluid density, $\mathbf{g}$ is the gravitational acceleration vector, ϕ is the matrix porosity, c_f is the fluid compressibility, K_s is the bulk modulus of the solid

grains, β_f is the fluid's volumetric thermal expansion coefficient, T_m is the matrix temperature, and c_L is the fluid leakoff coefficient. The fluid leakoff coefficient couples the two flow models and is defined as $c_L = k_n / \mu_f \delta$ where k_n is the permeability in the direction normal to the fracture and δ is the half-width of the element adjacent to the fracture (Salimzadeh and Khalili, 2015).

Fluid flow through the fracture's walls under nonisothermal conditions is modeled independently by the governing equation of the second flow model as (Zimmerman and Bodvarsson, 1996)

$$\iint_{\Gamma_c} \text{div}\left(\frac{a_f^3}{12\mu_f}\nabla p_f\right)dS = \iint_{\Gamma_c} \left[\frac{\partial \alpha_f}{\partial t} + \alpha_f c_f \frac{\partial p_f}{\partial t} - \alpha_f \beta_f \frac{\partial T_f}{\partial t} - c_L(p_m - p_f)\right]dS$$

(1.3)

where α_f is the aperture of the fracture and T_f is the temperature of fluid in the fracture (Salimzadeh et al., 2016a).

There are three heat transfer models: the solid, the fractures, and the rock matrix (Khalili and Selvadurai, 2003). The heat transfer model describing heat transfer through the deformable rock solid is governed by

$$\iiint_{\Omega} \text{div}(\lambda_s \nabla T_s)dV$$

$$= \iiint_{\Omega} \left\{\rho_s c_s \frac{\partial T_s}{\partial t} + \beta_s K T_s \frac{\partial(\text{div}\mathbf{u})}{\partial t} + c_{T_m}(T_s - T_m)\right\}dV + \iint_{\Gamma_c} c_{T_f}(T_s - T_f)dS$$

(1.4)

where λ_s is the thermal conductivity tensor of the solid, ρ_s is the solid density, c_s is the solid specific heat capacity, c_{T_m} is the solid-matrix heat exchange coefficient, and c_{T_f} is the solid-fracture heat exchange coefficient. Heat exchange between the solid and matrix or fracture is modeled by a thin, thermally resistive layer, such that the heat exchange coefficient is given by $c_{T_f} = \lambda_n / \delta$, where λ_n is the thermal conductivity in the direction normal to the fracture and δ is the half-width of the element adjacent to the fracture.

Similarly, the second heat model for heat transfer through the fracturing fluid is governed by

$$\iiint_{\Gamma} \text{div}(\alpha_f \lambda_f \nabla T_f)dV = \iint_{\Gamma_c} \left[\alpha_f \rho_f C_f \frac{\partial T_f}{\partial t} - \alpha_f \beta_f T_f \frac{\partial p_f}{\partial t}\right]dS$$

$$+ \iint_{\Gamma_c} [\alpha_f \rho_f C_f \mathbf{v}_f \cdot \nabla T_f + c_{T_f}(T_f - T_s) + \rho_f C_f c_L(p_m - p_f)(T_f - T_m)]dS$$

(1.5)

where λ_f is the isotropic thermal conductivity tensor of the fluid, C_f is the heat capacity of the fluid, and $\mathbf{v}_f$ is the velocity vector of the fluid in the fracture.

Finally, the third heat model, for matrix heat transfer, is governed by the following equation:

$$\iiint_{\Omega} \text{div}(\boldsymbol{\lambda}_f \nabla T_m) dV = \iint_{\Gamma_c} \rho_f c_L C_f (p_m - p_f)(T_m - T_f) dS$$

$$= \iiint_{\Omega} \left\{ \phi \rho_f C_f \frac{\partial T_m}{\partial t} - \phi \beta_f T_m \frac{\partial p_m}{\partial t} + \phi \rho_f C_f \mathbf{v}_m \cdot \nabla T_m + c_{T_m}(T_m - T_s) \right\} dV$$

$$\tag{1.6}$$

where $\mathbf{v}_f$ is the velocity vector of the fluid in the matrix.

The above equations are solved using the finite-element method for the spatial discretization of the equations and using the finite difference technique for the temporal discretization. To apply these methods, the domain is discretized into a hybrid volumetric-surface mesh that contains both quadratic tetrahedra and triangles.

The procedures and equations described in this work have been implemented into the Geomechanics module (Paluszny and Zimmerman, 2011; Salimzadeh et al., 2017a,b) of the Complex System Modeling Platform (CSMP++), an object-oriented finite element−based API-developed platform for the simulation of complex geological processes (Matthäi et al., 2001). The system of equations resulting from the finite-element method accumulation is solved using the Fraunhofer SAMG Solver library (Stüben, 2001).

Contact between fracture surfaces is modeled using a gap-based augmented Lagrangian approach that resolves the stresses on the fracture surfaces as a function of the local compressive forces, in an iterative manner (Nejati et al., 2016). Thus, under compression the fracture walls are prevented from interpenetration by resolving the frictional forces on fracture walls. Contact resolution is solved iteratively and requires the solution to a nonlinear problem that is solved using the Uzawa algorithm (Nejati et al., 2016). Contact and THM solutions are solved sequentially, thus, for each iteration, one contact and one THM step are solved before the iteration is evaluated.

1.4 MODELING DISCRETE FRACTURE GROWTH

Modal SIFs are computed by evaluating the I-integral over a virtual disk domain (Nejati et al., 2015a). An alternative, displacement correlation technique is also applied side-by-side, for comparison purposes (Nejati et al., 2015b). The mixed-mode three-dimensional Schöllmann method (Schöllmann et al., 2002) is used to compute the growth angle. At each growth iteration, growth vectors are constructed so as to capture changes to the fracture geometry. Growth vectors are translated into the deformation of the fracture surface, or the addition of new fracture surfaces/triangles to the original geometry. As a result, the fracture geometry adapts to the stress state, and the

geometry of the fracture network effectively changes and adapts to the stress state. Thereafter, the mesh is adaptively refined to the new geometry, following the new fracture surface.

Capturing the stress singularity ahead of the fracture tip is the key to accurately estimating the SIFs. Isoparametric quadratic tetrahedra and triangles are defined around the crack tips to capture the $1/\sqrt{r}$ stress and displacement singularities. As the low and displacement equations are solved in a monolithic fully coupled approach, only one type of element is used, and both flow and displacement are computed on isoparametric quadratic elements. Each tip curve is discretized into a set of tip segments. SIFs, for modes I, II, and III, are computed for each segment of the fracture tip.

The SIFs, for modes I, II, and III, can be related to the J-integral, which quantifies the amount of energy released to extend the fracture tip for unit length in the direction of the crack plane (Paluszny and Zimmerman, 2011), defined as

$$J = \frac{1}{A_c} \iiint\limits_{V_c} \left(\sigma_{ij} \frac{\partial u_j}{\partial x_k} - W \delta_{ik} \right) \frac{\partial q_k}{\partial x_i} dV, \tag{1.7}$$

where A_c is the amount of fracture surface area created by an extension of the fracture that increases by extension, V_c is the volume of the virtual unit cylinder over which J is computed, W is the strain energy density, δ_{ik} is the Kronecker delta, and q_k is an arbitrary weighting vector that represents the virtual crack extension.

The SIF K is then related to J by

$$J = K^2 / E_{eff}, \tag{1.8}$$

where E_{eff} is computed from the Young's modulus E, Poisson's ratio $\acute{\iota}$, and the local principal strains $\{\varepsilon_x, \varepsilon_y, \varepsilon_z\}$ as follows:

$$E_{eff} = E \left[\frac{1}{1 - \nu^2} + \frac{\nu}{1 + \nu} \left(\frac{\varepsilon_z}{\varepsilon_x + \varepsilon_y} \right) \right]. \tag{1.9}$$

There are three different SIFs, which correspond to different deformation modes: K_{I} for the opening mode (mode I), K_{II} for the in-plane shear mode (mode II), and K_{III} for the out-of-plane shear mode (mode III).

Three criteria are needed to model the propagation of the fractures based on the SIFs calculated around the tip: the failure criterion, the propagation magnitude criterion, and the propagation angle criterion. The failure criterion can be expressed as

$$K_v > K_{Ic}, \tag{1.10}$$

where K_{Ic} is the critical SIF, i.e., the rock's "toughness." The term K_v is the component of the SIF in the propagation direction and is given by

$$K_v = \frac{1}{2} \cos(\varphi_0/2) \left[K_{cs} + \sqrt{K_{cs}^2 + 4K_{\mathrm{III}}^2} \right], \tag{1.11}$$

where $K_{cs} = K_I \cos^2(\varphi_0/2) - (3/2)K_{II} \sin \varphi_0$. The term φ_0 is the deflection angle, which is perpendicular to the crack tip (Schöllmann et al., 2002). At every time step of the simulation, the SIFs $\{K_I, K_{II}, K_{III}, K_v\}$ are calculated at each discretized crack tip and then compared against the rock toughness K_{Ic}. Any tips that have K_v values exceeding the rock toughness K_{Ic} are considered to have a failure, after which the fracture tip is extended by a specific extension length that is defined at the beginning of the simulation. To avoid unnecessary growth steps, and considering that the matrix is homogenous, when K_v at one tip reaches K_{Ic} (i.e., growing is triggered), all other tips that have $K_v > 0.3 K_{Ic}$ are extended as well. The fracture extension angle is then calculated for these tips based on the propagation angle criterion that allows determining the new ridgeline of fracture tips and updated surface. Once the geometry is updated after each growth step, the model is outsourced to an octree volumetric mesher, and remeshing is done for the entire model.

1.5 EFFECT OF MATRIX POROELASTICITY ON THE GROWTH OF A SINGLE FRACTURE

Analytical methods are able to shed light on specific cases of hydraulic fracture growth, such as the viscosity-dominated, storage-dominated, toughness-dominated, and leakoff-dominated regimes, whereas numerical models are able to handle intermediate regimes (Salimzadeh et al., 2017a,b). The constitutive behavior of the matrix plays an important role in predicting fracture growth in both permeable and impermeable rock formations. In particular, for permeable formations, effects of matrix poroelasticity should not be neglected, as they influence the predicted aperture and lateral extent of the fracture. For toughness-dominated cases, decoupled numerical simulations of hydraulic fracture growth in both permeable and impermeable formations overestimate both fracture apertures and radii during injection. In the case of impermeable formations, the storage-toughness (Savitski and Detournay, 2002) and leakoff-toughness (Bunger et al., 2005) asymptotic solutions provide upper and lower bounds, respectively, to the fracture radii and apertures (Fig. 1.4). In contrast, for permeable formations, the analytical solution for the storage-toughness regime provides an upper bound for both the fracture radii and aperture, but the leakoff-toughness solution fails to provide a lower boundary for the same fracture parameters.

1.6 EFFECT OF INTERACTION ON THE PATHS OF TWO FLUID-DRIVEN PENNY-SHAPED CRACKS

The fluid-driven growth of a single fracture is governed by the interplay between deformation and flow that determines the stress concentrations at the fracture tip. Growth is often examined as a function of in situ or remote stresses, therefore, the far-field stress state is assumed to control the growth of

(A)

(B)
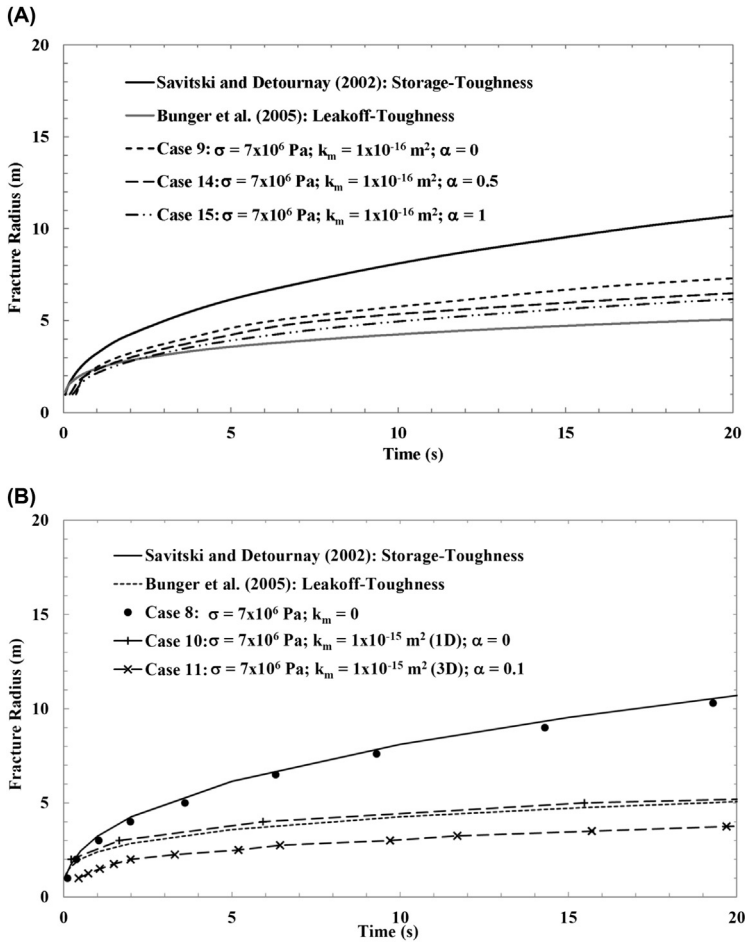
FIGURE 1.4 Fracture radius as a function of time for different regimes, for varying Biot co-efficients, for (A) a low permeability matrix and (B) a permeable matrix. Notice how the storage-toughness and leakoff-toughness asymptotic solutions provide bounds for the low permeability matrix case only.

the fractures. However, in cases when more than one fracture grows simultaneously, fractures also interact with each other during growth. Matrix permeability, spacing (Roussel and Sharma, 2011), preexisting fractures (Cruz et al., 2016), geology and matrix heterogeneity (Izadi et al., 2017) are expected to influence the interaction. During simultaneous growth, fractures exert a compressive shadow (Fischer et al., 2004) that influences their curving, and in turn, influence how far they grow into the formation.

First, the case of two penny-shaped cracks is investigated. The cracks are at a fixed spacing and grow simultaneously during fluid injection. The two
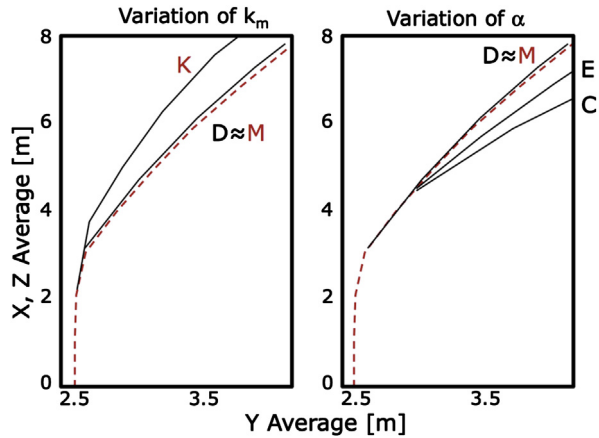
FIGURE 1.5 Fracture paths of an interacting fracture as a function of varying Biot coefficient. As the fracture grows, it deflects from its original plane, in the direction away from the neighboring fracture (see Table 1.1 for properties of cases).

fractures grow along a horizontal well and are under isotropic compressive in situ stresses. Interaction is observed for fractures that grow at a spacing of less than five times their radius, for both permeable and impermeable formations. As fractures interact, they curve away from each other and depart from their original plane of growth (Fig. 1.5). For an impermeable matrix, with $k_m = 0$ m^2, and a higher permeability matrix with $k_m = 2 \times 10^{-13}$ m^2, the

TABLE 1.1 Biot Coefficient, Permeability, Horizontal and Vertical Stresses, and Spacing Values Assigned for Simulation Runs

ID	Regime	Biot α (-)	k_x, k_y, k_z (m^2)	σ_H, σ_v (MPa)	σ_h (MPa)	Spacing l (m)
M	Viscosity-storage	0	0	20	20	5
K	Toughness-storage	0	0	20	20	5
C	Viscosity-leakoff	1	2×10^{-13}	20	20	5
D	Viscosity-leakoff	0	2×10^{-13}	20	20	5
E	Viscosity-leakoff	0.4	2×10^{-13}	20	20	5

paths are affected by fluid leakoff from the fracture to the matrix. As compared to the impermeable case, fracture interaction in permeable media is more prominent. Thus, fracture interaction is enhanced by the effect of the fluid leaking from the fracture into the adjacent rock formation.

For a higher permeability matrix, 2×10^{-13} m^2, the effect of the rock's poroelastic deformation is investigated. For the hypothetical case in which the Biot coefficient is 0, mechanical and flow simulations are decoupled. This case is unrealistic, as the Biot coefficient would always be higher than the rock porosity (Zimmerman, 2000), but can be investigated to highlight the differences between the permeable and impermeable cases. This case is closest to the impermeable matrix base case, and it represents a scenario under which leakoff does not affect the aperture of the fracture or its growth. For a somewhat higher Biot coefficient of 0.4, the leakoff effect is noticeable, and the interaction effect is increased. For the extreme case of a Biot coefficient of 1, the interaction effect is further increased.

It is worth noting that the differences in fracture paths occur most strongly at the onset of fracture propagation, when the distance between the tips of two adjacent fractures is smallest. For the impermeable cases (M and K), the fracture deviates around 11 degrees from the vertical axis at the onset of growth, whereas for the high and low permeable cases (M and K, respectively; $\alpha = 0$), additional deviations are 19 and 32 degrees, respectively. Once the course of the fracture is set, the path does not undergo significant changes. In contrast, for the poroelastic cases, the difference in angle is much less pronounced (8 and 6 degrees, respectively), as the ensuing paths continue to diverge as the fractures grow. This indicates that permeability and poroelasticity are complementary mechanisms affecting the interaction between fractures, affecting growth at both onset and development of the hydraulic fractures.

In an array of simultaneously stimulated fractures that contains more than two fractures, the interplay of fracture interaction has effects that go beyond the curving of the fracture paths (Fig. 1.6). Five fractures of 1 m radius, initially spaced at 3 m, in a $100 \times 90 \times 90$ m box are stimulated at an injection rate of $Q = 0.005$ m^3/s, for hydrostatic ($\sigma_h = \sigma_H = \sigma_v = 10$ MPa) and nonhydrostatic far-field stress states ($\sigma_h = 10$ MPa, $\sigma_H = 11$ MPa, $\sigma_v = 12$ MPa). For a fixed fracture spacing, fracture interaction depends on the in situ conditions and influences both the fracture paths and the fracture apertures. For isotropic in situ stresses, the boundary fractures exhibit strong deflection from the original path. For the case of the nonisotropic in situ stresses, fractures at the extremes of the array exhibit less curving. For anisotropic stress conditions, the middle fractures are observed to grow further than they would in the isotropic case and sustain larger apertures in the center fracture. For fractures that are stimulated sequentially, curving is also observed to depend on the in situ stresses (Salimzadeh et al., 2017b).
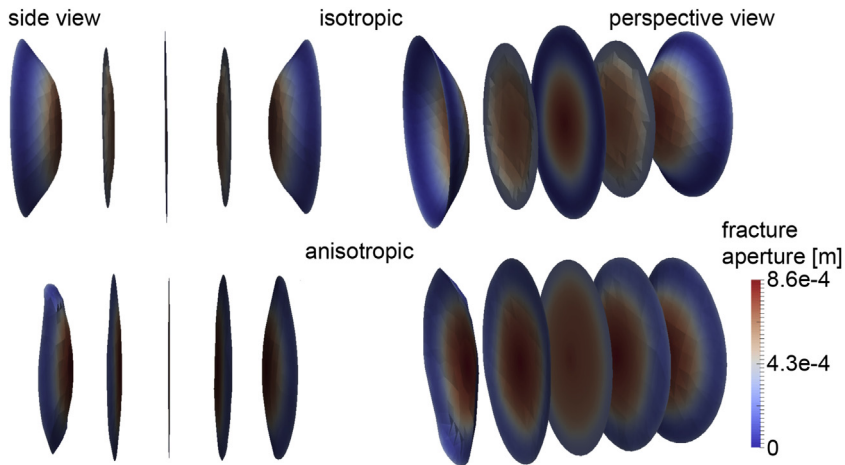
FIGURE 1.6 Five fractures interact during growth for isotropic (top) and anisotropic (bottom) boundary conditions.

1.7 THERMAL EFFECTS ON EARLY STAGES OF HYDRAULIC FRACTURE GROWTH

During hydraulic fracturing, the temperature of the injected fluid is often much lower than that of the matrix rock. Due to thermomechanical coupling in the rock mass, it is expected that this temperature difference may influence stresses at the tip of the fracture and thereby influence the rate of fracture growth. However, the small volume of fluid contained in the fracture quickly enters equilibrium with the rock, and thus, the temperature contrast fails to cause any additional strains in the short term.

Although analytical solutions have been developed for simple scenarios, they do not generally account for processes such as heat transfer between the fracturing fluid and the rock mass or leak-off into a poroelastic rock mass. Thermal effects of the hydraulic fracturing process can be studied numerically, accounting for heat transfer through the solid rock and the fracturing fluid, and for the transfer of thermal energy between the rock and fluid. Fractures provide highly conductive channels, rapidly transferring heat through the formation. In contrast, heat transfer through the solid rock is usually slow and largely independent of the hydraulic properties of the matrix.

Local thermal nonequilibrium between fracture fluid and neighboring rocks leads to heat transfer between them. The rate of heat transfer depends on the temperature differences, as well as the thermal properties of the rock.

Hydraulic fracturing is investigated for local thermal nonequilibrium in an impermeable matrix. Water is injected at a temperature $100°C$ cooler than the formation, at an injection rate $Q = 0.001 \text{ m}^3/\text{s}$, with a viscosity $/ = 0.1$ Pa s, and a fracture toughness $K_{Ic} = 1 \text{ MPa m}^{0.5}$.

(A)

(B)
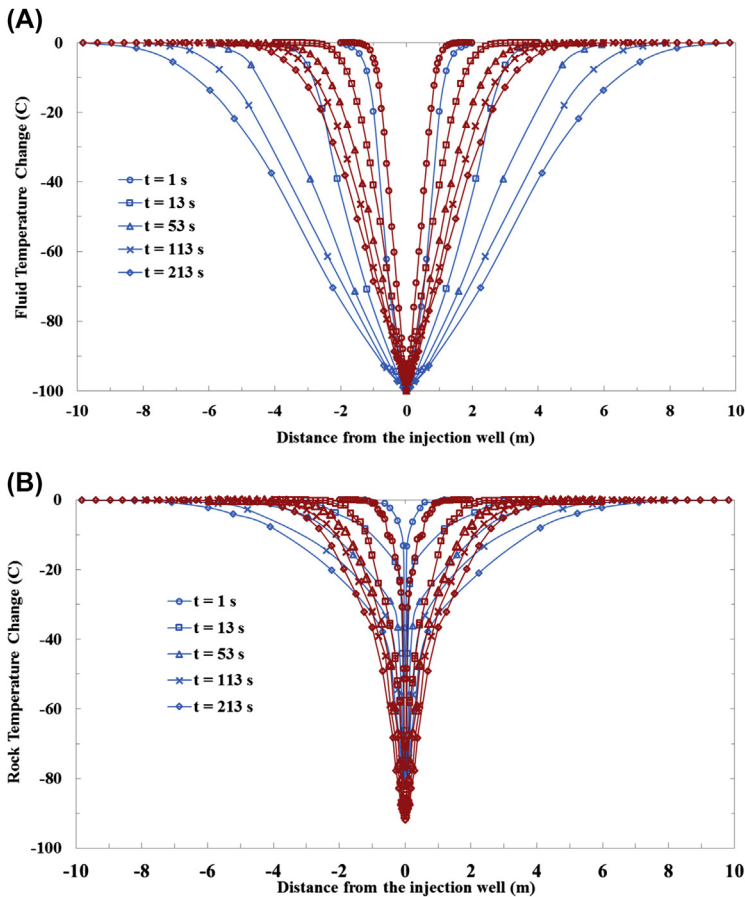
FIGURE 1.7 Temperature change as a function of matrix diffusivity. In blue (light gray in print versions), with a lower value of thermal diffusivity, 1×10^{-6} m^2/s; and in red (dark gray in print versions), with a higher thermal diffusivity, 1×10^{-5} m^2/s. In (A) fluid and (B) rock, temperature change as a function of distance to the injection point, and its progression over injection time (1, 13, 53, 113, and 213 s).

The temperature change along the radial distance along the fracture is plotted as a function of injection time in Fig. 1.7. Two cases are modeled: in blue, with a lower value of thermal diffusivity, 1×10^{-6} m^2/s; and in red, with a higher thermal diffusivity, 1×10^{-5} m^2/s. The initial radius of the fracture is 1 m, and reaches 8 m within the first 150 s of injection. Within this injection window, the large temperature contrast between fluid and rock is rapidly equilibrated as the fluid travels through the fracture. This rapid equilibration is assumed to be primarily due to the small volume of cooler fluid in the fracture. The results show that the thermal diffusivity has a significant effect on the speed at which the fluid temperature reaches equilibrium, with a lower rock

diffusivity causing the fluid to maintain its low temperature for longer. However, in both cases the fluid quickly equilibrates with the rock over the length of the fracture; and in both cases thermal diffusivity does not substantially influence the temperature change of the rock. The temperature contrast between fluid and rock causes local contraction of the rock, occurring most significantly in the vicinity of the well (Salimzadeh et al., 2016).

The effect of the injection rate on the temperature change in the fluid and rock is plotted in Fig. 1.8. In the image, blue represents a lower value of injection rate, $Q = 0.001$ m³/s, and red depicts a higher injection rate, $Q = 0.01$ m³/s. Higher
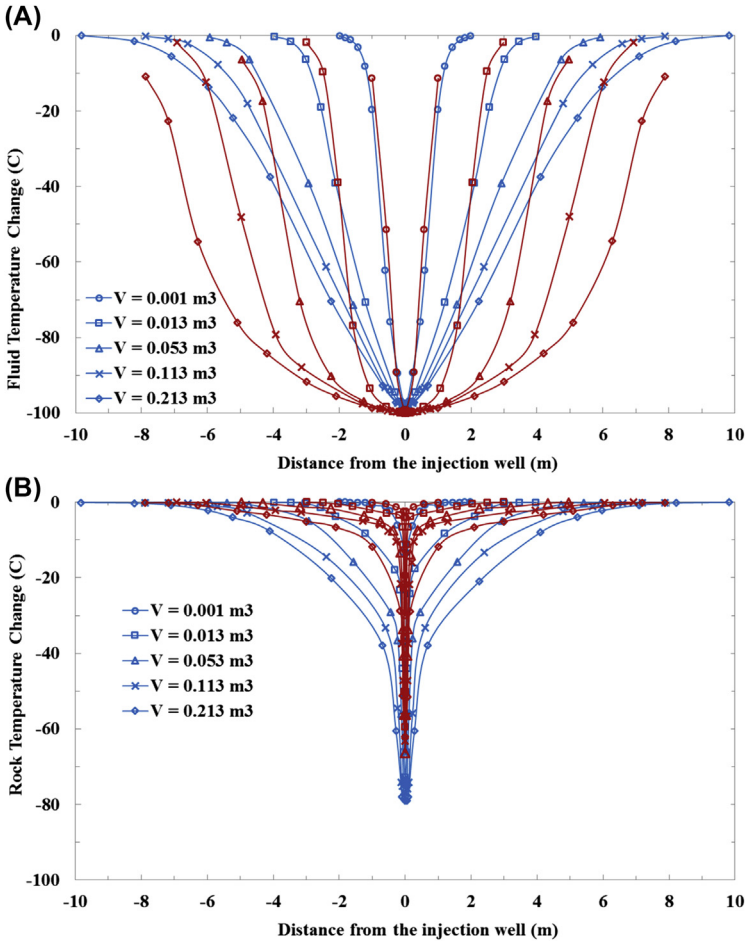

FIGURE 1.8 Temperature change as a function of injection rate. In blue (light gray in print versions), with a lower value of injection rate $Q = 0.001$ m³/s; and in red (dark gray in print versions), with a higher injection rate, $Q = 0.01$ m³/s. In (A) fluid and (B) rock, temperature change as a function of distance to the injection point, and its progression over injection volume.

injection rates push the fluids through the system at a higher velocity; therefore, fluids conserve their original temperature during injection and are slower to equilibrate, as compared with the lower injection rate case.

However, for the same amount of injected fluid volume, the rock will undergo much less cooling in the case of the high injection rate, as opposed to the low injection rate case. Thus, larger fracture radii can be achieved with a smaller temperature change.

These results show that temperature contrast does cause a temperature gradient inside the fracture, which is nonlinear, and depends both on the rock diffusivity and the injection rate. An assumption of constant temperature within the fracture may lead to the overestimation of the effect of cold injection on rock contraction and in turn, may overpredict fracture growth enhancement (Usui, 2016).

1.8 CONCLUSIONS

An advanced numerical framework has been presented to model the growth of multiple discrete fractures as a result of the porothermoelastic deformation of a porous matrix. The approach is based on the finite-element method and has been applied to study the effects of matrix permeability, poroelastic behavior of the matrix, and fluid injection temperature, on the overall growth of the fractures. Results highlight the importance of poroelastic and permeability effects, by illustrating the effects of matrix deformation and leakoff on the resultant fracture radii and apertures. For the particular cases investigated herein, we find that matrix cooling during cold injections has a negligible effect on fracture growth at the onset of injection and mainly affects the apertures in the vicinity of the injection well. This analysis is based on very short injection periods and focuses only on the fracturing that takes place at the onset of cold injection. As opposed to asymptotic analytical solutions, the presented simulations can assess a wider variety of geometric settings, and can evaluate complex boundary conditions and reservoir settings that are closer to realistic conditions. The computational framework is flexible and can be adapted to accommodate other constitutive models for the rock and the fluid.

REFERENCES

Bordas, S., Rabczuk, T., Zi, G., 2008. Three-dimensional crack initiation, propagation, branching and junction in non-linear materials by an extended mesh-free method without asymptotic enrichment. Engineering Fracture Mechanics 75 (5), 943−960.

Bunger, A.P., Detournay, E., Garagash, D.I., 2005. Toughness-dominated hydraulic fracture with leak-off. International Journal of Fracture 134, 175−190.

Carter, B.J., Wawrzynek, P.A., Ingraffea, A.R., 2000. Automated 3D crack growth simulation. International Journal of Numerical Methods in Engineering 47, 229−253.

Cruz, L., Izadi, G., Moos, D., Sheridan, J., Fu, P., Settgast, R.R., Ryerson, F.J., 2016. The role of natural fractures (joints) in the Marcellus shale during hydraulic fracture stimulation using full 3D modeling. In: Unconventional Resources Technology Conference, San Antonio, Texas, August 1–3, 2016, pp. 1049–1061.

Fisher, M.K., Heinze, J.R., Harris, C.D., Davidson, B.M., Wright, C.A., Dunn, K.P., 2004. Optimizing horizontal completion techniques in the Barnett shale using microseismic fracture mapping. In: Paper SPE 90051. SPE Annual Technical Conference and Exhibition, Houston, September 26–29, 2004.

Izadi, G., Moos, D., Cruz, L., Gaither, M., Chiaramonte, L., Johnson, S., 2017. Fully coupled 3-D hydraulic fracture growth in the presence of weak horizontal interfaces. In: Society of Petroleum Engineers. SPE Hydraulic Fracturing Technology Conference and Exhibition, January 24–26, 2017, The Woodlands, Texas, USA.

Khalili, N., Selvadurai, A.P.S., 2003. A fully coupled constitutive model for thermo-hydro-mechanical analysis in elastic media with double porosity. Geophysical Research Letters 30 (24), 2268.

Lazarus, V., 2003. Brittle fracture and fatigue propagation paths of 3D plane cracks under uniform remote tensile loading. International Journal of Fracture 122, 23–46.

Matthäi, S.K., Geiger, S., Roberts, S.G., 2001. The Complex Systems Platform csp3.0: Users Guide. Technical report, ETH Zürich Research Reports.

Nejati, M., Paluszny, A., Zimmerman, R.W., 2015a. A disk-shaped domain integral method for the computation of stress intensity factors using tetrahedral meshes,. International Journal of Solids and Structures 69–70, 230–251.

Nejati, M., Paluszny, A., Zimmerman, R.W., 2015b. On the use of quarter-point tetrahedral finite elements in linear elastic fracture mechanics. Engineering Fracture Mechanics 144, 194–221.

Nejati, M., Paluszny, A., Zimmerman, R.W., 2016. A finite element framework for modeling internal frictional contact in three-dimensional fractured media using unstructured tetrahedral meshes. Computer Methods in Applied Mechanics and Engineering 306, 123–150.

Paluszny, A., Matthai, S.K., Hohmeyer, M., 2007. Hybrid finite element-finite volume discretization of complex geologic structures and a new simulation workflow demonstrated on fractured rocks. Geofluids 7 (2), 186–208.

Paluszny, A., Zimmerman, R.W., 2011. Numerical simulation of multiple 3D fracture propagation using arbitrary meshes. Computer Methods in Applied Mechanics and Engineering 200 (9–12), 953–966.

Paluszny, A., Zimmerman, R.W., 2013. Numerical fracture growth modeling using smooth surface geometric deformation. Engineering Fracture Mechanics 108, 19–36.

Patzak, B., Jirasek, M., 2004. Adaptive resolution of localized damage in quasibrittle materials. ASCE Journal of Engineering Mechanics 130, 720–732.

Rabczuk, T., Belytschko, T., 2007. A three-dimensional large deformation meshfree method for arbitrary evolving cracks. Computer Methods in Applied Mechanics and Engineering 196 (29–30), 2777–2799.

Roussel, N.P., Sharma, M.M., 2011. Optimizing Fracture Spacing and Sequencing in Horizontal-well Fracturing. Society of Petroleum Engineers. Paper SPE 127986.

Salimzadeh, S., Paluszny, A., Zimmerman, R.W., 2016. Thermal effects during hydraulic fracturing in low-permeability brittle rocks. In: 50th US Rock Mechanics Symposium, Houston, June 26–29, 2016, Paper ARMA, pp. 16–368.

Salimzadeh, S., Paluszny, A., Zimmerman, R.W., 2017a. Three-dimensional poroelastic effects during hydraulic fracturing in permeable rocks. International Journal of Solids and Structures 108, 153–163.

Salimzadeh, S., Usui, T., Paluszny, A., Zimmerman, R.W., 2017b. Finite element simulations of interactions between multiple hydraulic fractures in a poroelastic rock. International Journal of Rock Mechanics & Mining Sciences 99, 9−20.

Salimzadeh, S., Khalili, N., 2015. A three-phase XFEM model for hydraulic fracturing with cohesive crack propagation,. Computers and Geotechnics 69, 82−92.

Savitski, A.A., Detournay, E., 2002. Propagation of a penny-shaped fluid-driven fracture in an impermeable rock: asymptotic solutions. International Journal of Solids and Structures 39, 6311−6337.

Schöllmann, M., Richard, H.A., Kullmer, G., et al., 2002. A new criterion for the prediction of crack development in multi-axially loaded structures. International Journal of Fracture 117 (2), 129−141.

Stüben, K., 2001. A review of algebraic multi-grid. Journal of Computational and Applied Mathematics 128, 281−309.

Usui, T., 2016. Effects of Poroelasticity on Hydraulic Fracture Interaction (M.Sc. thesis). Imperial College London.

Vernerey, F.J., Kabiri, M., 2014. Adaptive concurrent multiscale model for fracture and crack propagation in heterogeneous media. Computer Methods in Applied Mechanics and Engineering 276, 566−588.

Zimmerman, R.W., 2000. Coupling in poroelasticity and thermoelasticity. International Journal of Rock Mechanics & Mining Sciences 37, 79−87.

Zimmerman, R.W., Bodvarsson, G.S., 1996. Hydraulic conductivity of rock fractures. Transport in Porous Media 23, 1−30.